

# Real-time imaging and characterization of human breast tissue by reflectance confocal microscopy

**Maddalena T. Tilli**

**M. Carla Cabrera**

**Angela R. Parrish\***

**Kathleen M. Torre**

Lombardi Comprehensive Cancer Center  
Georgetown University  
Washington, D.C. 20057

**Mary K. Sidawy**

Georgetown University  
Department of Pathology  
Washington, D.C. 20057

**Ann L. Gallagher**

Lombardi Comprehensive Cancer Center  
Georgetown University  
Washington, D.C. 20057

**Erini Makariou**

**Sandra A. Polin**

Georgetown University  
Department of Radiology  
Washington, D.C. 20057

**Minetta C. Liu<sup>†</sup>**

**Priscilla A. Furth<sup>†</sup>**

Lombardi Comprehensive Cancer Center  
Georgetown University  
Washington, D.C. 20057

## 1 Introduction

Near-infrared reflectance confocal microscopy (RCM) (VivaCell-TiBa, Rochester, New York) has the potential to make a significant contribution to the advancement of screening and diagnosis, especially for the early detection of precancerous lesions.<sup>1-9</sup> Unlike traditional microscopy, RCM allows 3-D optical sectioning of opaque objects, such as *in-vivo* (living) or *ex-vivo* (newly biopsied) human tissue. A thin plane can be noninvasively imaged with high resolution and contrast without the use of time-consuming and potentially destructive fixation and staining, both of which may introduce artifacts and damage tissue.<sup>5,7</sup> Images are obtained in real time by detecting local variations in the refractivity of cellular and subcellular structures in their native state. For example, this technique has been used to characterize cellular detail of the

**Abstract.** Real-time technologies can increase the efficiency of obtaining informative biopsies and accelerate interpretation of biopsy pathological review. Cellular aberrations inherent to cancer cells, including nuclear size, can currently be detected, but few technologies are available to evaluate adequacy of specimens in real time. The aims of this study are: 1. to determine if near-infrared reflectance confocal microscopy (RCM) can be used to assess epithelial/stromal content of core needle breast biopsy samples in real time, 2. to determine if epithelial cell nuclear size can be measured on RCM images, and 3. to test if RCM images can be accurately read for presence/absence of histologically relevant features of malignancy. Breast biopsies are obtained following a medically indicated breast core needle diagnostic biopsy for RCM examination. Acetic acid is used as a contrast agent to visualize structures within breast tissue. Structures are identified and optically serially sectioned, and digital images are cataloged. Relative amounts of epithelial, fatty, and collagenous tissue are determined. RCM biopsies are formalin-fixed and stained for hematoxylin and eosin (H and E) comparison with RCM images. RCM data are comparable to data from H and E sections. Epithelial cell nuclear size is measured on stored digital RCM images. We compare RCM and H and E images from 16 patients and 25 core needle biopsy samples. © 2007 Society of Photo-Optical Instrumentation Engineers. [DOI: 10.1117/1.2799187]

**Keywords:** breast cancer; reflectance confocal microscopy; real-time imaging; non-destructive pathology; breast biopsy; core needle biopsy.

Paper 07043SSR received Feb. 5, 2007; revised manuscript received Jun. 10, 2007; accepted for publication Jun. 11, 2007; published online Oct. 29, 2007.

retina<sup>10</sup> and cornea,<sup>11</sup> normal<sup>12</sup> and neoplastic<sup>3</sup> oral mucosa, normal and diseased parathyroid glands,<sup>1</sup> normal skin,<sup>13</sup> and dermatitis.<sup>6</sup> RCM is currently being used to noninvasively diagnose dermatological conditions such as basal cell carcinoma, melanocytic, and nonmelanoma skin tumors.<sup>5,14,15</sup> Campo-Ruiz et al. also show that RCM of freshly excised hepatic specimens can depict cellular and subcellular detail and distinguish morphological features of diseased and normal hepatic tissue.<sup>2</sup>

RCM has been used to identify cancer within a tissue. Hallmarks of precancerous cervical cancer such as increased nuclear size and increased nuclear:cytoplasmic ratio are characteristics that can be assessed by RCM, and have been used successfully to detect high-grade cervical dysplasia with high specificity and sensitivity.<sup>16</sup> High sensitivity and specificity were also shown in the diagnosis of melanocytic skin tumors from benign nevi using cytomorphology and architecture on RCM images,<sup>17</sup> and in the diagnosis of basal cell carcinoma using the presence of elongated nuclei on RCM images.<sup>18</sup> Additional studies have demonstrated that RCM can be used for real-time assessments of tumor margins,<sup>7,19</sup> as well as to

Address all correspondence to Maddalena Tilli, Lombardi Comprehensive Cancer Center, Georgetown University, 3970 Reservoir Rd NW-Research Bldg 521A, Washington, DC 20057 United States of America; Tel: 202 687 8682; Fax 202 687 7505; E-mail: mtt7@georgetown.edu

\*Current affiliation: The Salk Institute for Biological Studies, The Jack H. Skirball Center for Chemical and Biological Studies, 10010 N. Torrey Pines Rd., La Jolla, CA 92037.

<sup>†</sup>Contributed equally.

rapidly obtain serial images of different skin lesions to evaluate dynamic pathophysiological responses to treatment.<sup>20,21</sup> Optical technologies such as RCM could help to eliminate unnecessary biopsies and treatments, decrease the cost of screening, increase sensitivity and specificity, and reduce treatment delays and disease recurrences by better assessment of tumor margins.<sup>4</sup>

Previously we have shown RCM to be very useful in optical serial imaging of normal mammary gland ductal structures and tumors from genetically engineered mice.<sup>22</sup> In the present study, we used mice to examine the utility of RCM to accurately image all stages of normal mammary gland development from puberty through pregnancy, lactation, and involution. Once this was established, we then went on to test if RCM could be successfully employed to study the structure of tissue from human breast core needle biopsies. Using these human specimens, we determined that this imaging technique was useful in assessing epithelial/stromal content and in assessing the presence/absence of histologically relevant features of malignancy in real time.

## 2 Materials and Methods

### 2.1 Reflectance Confocal Microscopy Imaging

RCM is an optical imaging technique that provides digital images of nuclear and cellular morphology of freshly excised tissue specimens. The VivaCell 5000 used in the current study uses an 830-nm wavelength infrared laser diode. This wavelength was investigated in confocal imaging of skin and found to provide a reasonable trade-off between image resolution and maximum imaging depth.<sup>23</sup> The light is circularly polarized, which improves the throughput of the system by nearly a factor of 4. Additional details about the optics involved has been described by Rajadhyaksha and Zavislan.<sup>24</sup> In brief, the optical path begins with the scanning optics, which illuminate a spot within the tissue with a point of light inside the specimen to be imaged. Intracellular and extracellular constituents cause a backscattering (reflection) of light, which is reflected onto a detector, creating an image. This backscattering of light is the result of refractive-index differences in various organelles and other structures. A pinhole placed in front of the detector filters out backscattered light both above and below the plane of the illuminated spot in the tissue, which would be out of focus. The result is a high-contrast image of an optical vertical section with a thickness of less than 5  $\mu\text{m}$  (comparable to histology) and a horizontal section thickness of 0.5 to 1.0  $\mu\text{m}$ . Tissue samples were pretreated with acetic acid to enhance reflectivity of the cell nuclei with increased DNA content.<sup>25,26</sup>

The VivaCell 5000 software can acquire high resolution digital images of  $500 \times 500 \mu\text{m}$  ( $1000 \times 1000$  pixels) slices of mammary gland morphology and also allows for Z-stack imaging (VivaStack), which takes multiple images (each stack consists of 16 images) at 1.585- $\mu\text{m}$  increments vertically through structures. This feature was used to take three stacks of images through the entire terminal end bud structure (TEB) in Fig. 1(b). The stacks were analyzed using the volume viewer plug-in of the ImageJ software (Image Analysis and Processing in Java, the National Institutes of Health (NIH), Bethesda, Maryland),<sup>27</sup> which artificially colors the composite image from a combination of all the stacks of a structure [Fig.

1(c)] and produces a 3-D rendering of the stacks (examples of images from a 3-D movie are shown in Figs. 1(d)–1(i). VivaBlock, which provides six  $\text{mm}^2$ —square composites of horizontally tiled  $500 \times 500\text{-}\mu\text{m}$  images, was used to map large areas of interest, as described previously.<sup>22</sup>

### 2.2 Mouse Mammary Gland Development Specimens and Imaging

Mammary glands from wild-type female mice were examined by RCM analysis at different stages of mammary gland development: virgin, lactation (day 10), and involution (days 2, 4, 6, 8, and 10). Virgin mice were sacrificed at 5 weeks of age and nonpregnant females at three months of age. Lactation and involution specimens were obtained by setting up timed matings of 2- to 4-month-old wild-type female mice with wild-type males. Day 1 of pregnancy was indicated on observation of vaginal plug. Females were allowed to deliver pups (21 days of pregnancy) and lactate for 10 days. At this time, lactation specimens were collected. Additional female mice were then allowed to go through involution for 2, 4, 6, 8, or 10 days to examine mammary gland remodeling.

Upon necropsy, number 4 mammary glands of virgin, non-pregnant, lactation, and involution mice were harvested and subjected to hematoxylin and eosin (H and E) staining (see next) and the #3 mammary glands from the same animals were injected with 5% percent acetic acid in phosphate buffered saline (PBS). Acetic acid was used as a contrast agent to enhance visualization of the nuclei within cells by promoting condensation of nuclear material. After acetic acid injection, the harvested mammary gland was placed on the glass stage above the  $30\times$  water immersion lens of the VivaCell 5000 Reflectance Confocal Microscope (TiBa, Rochester, New York) and a glass microscope slide was placed over the gland to spread and apply even pressure, as previously described.<sup>22</sup> Ductal morphology was directly imaged using VivaCell 5000 with the VS2000ui imaging software (version vs006.00.11, Lucid, Incorporated, Rochester, New York).

Mammary glands that were not easily imaged because extensive fat content obstructed RCM images were exposed to Carnoy's fixative (60% ethanol, 30% chloroform, 10% glacial acetic acid) for 15 to 30 min. Carnoy's fixative is usually used to fix mammary gland whole mounts by dehydrating the glands, and was used effectively here to reduce the interference of fat in RCM imaging.

For comparison with RCM images, the number 4 mammary glands of these same mice were fixed in 10% buffered formalin overnight at 4°C and embedded in paraffin using standard techniques. Sections (5  $\mu\text{m}$ ) were stained with H and E to visualize ductal morphology. All procedures involving animals were performed in accordance with current federal [NIH National Institutes of Health Guide for the Care and Use of Laboratory Animals] and university guidelines, and were reviewed and approved by the Georgetown University Institutional Animal Use and Care Committee.

### 2.3 Estrogen Receptor Alpha Immunohistochemistry

Immunohistochemical detection of estrogen receptor alpha ( $\text{ER}\alpha$ ) expression in mammary epithelial cells of mammary glands either exposed to 5% acetic acid in PBS and imaged with RCM, or not exposed to acetic acid and not imaged, was

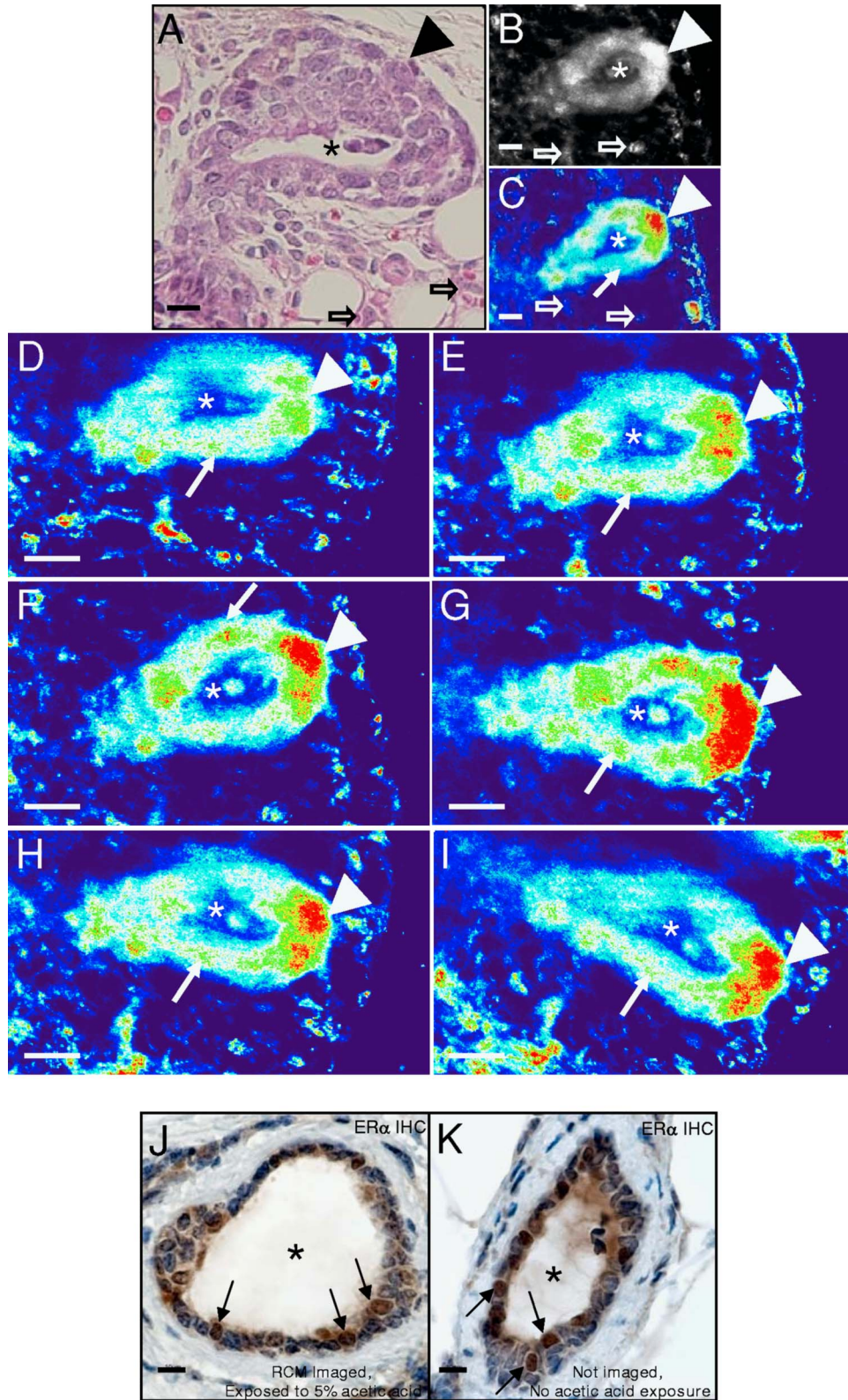


**Fig. 1** RCM can be used to image fundamental mouse mammary gland ductal morphology. (a) through (i) Terminal end bud (TEB) structures in the mammary gland of 5-week-old virgin wild-type females. (a) H and E stained image compared with (b) an RCM image from a different mouse. RCM image stacks of the TEB in (b) were artificially colored with the ImageJ software in (c) through (i). Representative points of interest indicated by arrowheads: proliferative cap cells of TEB, closed arrows: body cells of TEB, \*: lumen of TEB, open arrows: fat cell nuclei. Magnification: (a) =60 $\times$ , bar: 10  $\mu$ m; (b) through (i) =30 $\times$ , bar: 50  $\mu$ m. (j) and (k) ER $\alpha$  protein expression remains detectable by IHC in mouse mammary gland tissue after exposure to acetic acid. Representative images of ER $\alpha$  IHC in samples with (j) and without (k) exposure to acetic acid. Black arrows show mammary ductal epithelial cells that demonstrate positive nuclear localized ER $\alpha$  staining. Magnification: (j) and (k) =60 $\times$ , bar: 10  $\mu$ m.

performed as previously described.<sup>28</sup> Briefly, paraffin-embedded mammary gland tissue sections were deparaffinized, rehydrated, antigens exposed with high-pH target retrieval solution (S3307, DAKO, Carpinteria, California) and high temperature, and quenched with 3% hydrogen peroxide. Detection of ER $\alpha$  protein expression in mammary epithelial cells was accomplished using the Mouse on Mouse (MOM) peroxidase kit (PK-2200, Vector Laboratories, Incorporated, Burlingame, California) using a 1:50 dilution of the mouse monoclonal ER $\alpha$  antibody (IM2133, Beckman Coulter Immunotech, Miami, Florida) according to the manufacturer's directions. Sections were stained with the diaminobenzidine peroxidase (DAB) substrate kit (SK-4100, Vector Laboratories, Incorporated, Burlingame, California) for 5 min, counterstained with hematoxylin, and mounted with glycerol vinyl alcohol mount. Digital photographs of immunohistochemistry were taken using the Nikon Eclipse E800M microscope setup with Nikon DMX1200 camera and software (Nikon) with the 60 $\times$  objective.

## 2.4 Human Subjects

Eligible patients were recruited from two Institutional Review Board (IRB)-approved, clinical protocols that were designed specifically for the collection of core needle breast biopsies for correlative science studies. The majority of core biopsies are performed under ultrasound guidance to maximize yield. One protocol focuses on patients who require a diagnostic biopsy for a breast abnormality. The other protocol allows for serial breast tumor biopsies before and after the administration of neoadjuvant chemotherapy. Protocols for the RCM study were approved by the Institutional Review Board. Written informed consent for study participation was obtained from each subject, and all patient identifiers were removed to protect patient confidentiality.

## 2.5 Human Biopsy Imaging Procedures

After necessary diagnostic breast core needle biopsies were obtained, one to three additional biopsy samples were collected for RCM examination. Tissue targeted for RCM evaluation was immediately placed in PBS and imaged within 1 h of acquisition. Five percent acetic acid was injected into the tissue immediately prior to imaging. Structures within the entire  $\sim$ 12-mm-long and  $\sim$ 2-mm-thick breast specimen were imaged, visualized, identified, and optically serially sectioned, and digital images were cataloged within 5 to 10 min of injection. Relative amounts of epithelial, fatty, and collagenous tissue were determined.

## 2.6 Nuclear Size Measurement

Nuclear size was measured in normal mammary epithelial cells using Metamorph (Molecular Devices Corporation, Sunnydale, California). Only circular bright spots with a clearly defined circumference were measured. Measurements were obtained by drawing a straight line segment through the center of the nucleus by eye on a digital computer monitor, beginning and ending on the nuclear boundary. The distance (the diameter) was automatically calculated by Metamorph. 50 different nuclei were measured per field of view on each sample.

## 2.7 Pathological Evaluation

Following RCM imaging, biopsy samples were formalin-fixed, sectioned, and stained for H and E comparison with RCM images. Diagnoses were established on H and E stained sections by a board-certified pathologist with expertise in breast pathology (Sidawy), according to standard histopathological criteria. RCM images were matched with the H and E stained sections to directly compare imaging of the same tissue areas by the different techniques. Digital photographs of these areas on the H and E stained sections were taken.

# 3 Results and Discussion

## 3.1 Imaging Mouse Mammary Ductal Structures

Preclinical studies examining the utility of RCM for pathological definition of structural elements during different developmental and physiological states were performed on mouse mammary glands (Figs. 1 and 2). During puberty, the mouse mammary gland ductal structures extend through the fat pad to establish the ductal tree. The lead edge of the duct is a structure termed the terminal end bud (TEB), composed of proliferative cap cells and more differentiated body cells. Figure 1(a) shows an H and E stained section. Figure 1(b) shows an RCM image of the TEBs, where cap and body cells are indicated for comparison. NIH ImageJ was used to transfer the grayscale information from the stack of pictures taken of the entire structure in Fig. 1(b) into a broader color spectrum [Fig. 1(c)] and can be rotated in 3-D [Figs. 1(d)–1(i)] to more clearly highlight the changes in reflectance intensity as the stack goes through the different layers of the TEB. Acetic acid acts as a contrast agent by releasing histones that cause the formation of large DNA aggregates that are more reflective.<sup>25,26</sup> More reflective (brighter) spots on RCM indicate cell nuclei that have increased DNA content. Proliferative cells will demonstrate increased DNA content as the DNA is replicated prior to cell division. The cap cells (arrowheads) on the tip of the TEB are more proliferative, and therefore would be expected to be more reflective as demonstrated. In addition to ductal epithelial cells, the mouse mammary gland is also composed of fat cells. Fat cell nuclei (open arrows) are also reflective with RCM, although less reflective than the epithelial cell nuclei.

## 3.2 Tissue Treated with Acetic Acid Can be Used for Immunohistochemical Analyses

One of the benefits of RCM is thought to be the nondestructive nature of the technique. However, tissue samples must be treated with 1 to 5% acetic acid or another contrast agent prior to imaging. This process theoretically could affect the ability to detect common breast cancer biomarkers such as estrogen receptor alpha (ER $\alpha$ ). To determine if acetic acid treatment compromised immunohistochemical (IHC) detection of ER $\alpha$ , treated (RCM imaged) and untreated (not imaged) mammary tissues were probed for ER $\alpha$  protein using IHC and results compared. ER $\alpha$  protein expression remained detectable by IHC in the nucleus of ductal epithelial cells (arrows) of mouse mammary gland tissue after exposure to 5% acetic acid and RCM imaging [Fig. 1(j)] when compared to untreated, non-imaged tissue [Fig. 1(k)]. Therefore, the acetic acid treatment

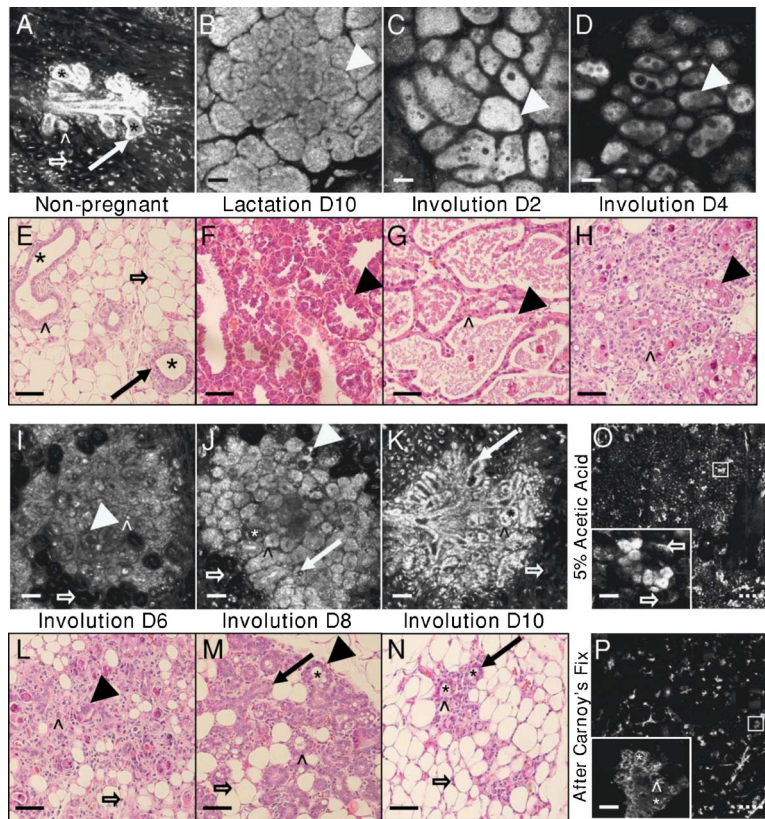


**Fig. 2** RCM can be used to image the mouse mammary gland during lactation and involution. Comparison of H and E (e) through (h) and (l) through (n) and RCM (a) through (d) and (i) through (k) images from nonpregnant (a) and (e), lactating (b) and (f), and involuting (c), (d), and (g) through (n) wild-type female mouse mammary glands. Vivablock map and closeup of boxed area (insert) comparing a fatty mammary gland (o) before and (p) after treatment with Carnoy's fixative. Representative points of interest indicated by closed arrows: mammary ducts, arrowheads: mammary lobules,  $\wedge$ : ductal epithelial cell nuclei, \*: lumen of duct, and open arrows: fat cell nuclei. Magnification: H and E=20 $\times$ , bar: 50  $\mu$ m; RCM [(a) through (d), (i) through (k), (o), and (p) inserts]=30 $\times$ , bar: 50  $\mu$ m; RCM (o) and (p) dotted bar (right): 500  $\mu$ m.

did not alter the integrity of the tissue, allowing for further analysis of proteins of interest to be performed on the treated tissue after RCM.

### 3.3 Comparing Reflectance Confocal Microscopy and Hematoxylin and Eosin Images of Mammary Glands During Pregnancy and Involution

Following lactation, the mammary gland is remodeled during a process termed involution. Epithelial cells undergo apoptosis while the stromal tissues are remodeled through the expression of various enzymes. Figure 2 demonstrates that the remodeling of the mammary gland from nonpregnant [Figs. 2(a) and 2(e)] to lactation [Figs. 2(b) and 2(f)] through involution [Figs. 2(c), 2(d), and 2(g)–2(n)] can be similarly appreciated with both H and E [Figs. 2(e)–2(h) and 2(l)–2(n)] and RCM [Figs. 2(a)–2(d) and 2(i)–2(k)]. During pregnancy and lactation, the ductal epithelial cells form lobular alveolar structures [Figs. 2(b) and 2(f), arrowhead] and differentiate into milk-secreting lobules during lactation, which at parturition produce milk.<sup>29</sup> After weaning, the mammary gland undergoes involution, where cell death and remodeling of the gland begins on involution day 2. By involution day 4, the alveolar epithelial cells begin to die, collapsing the alveoli into clusters of epithelial cells, and fat cells begin to reappear

[Figs. 2(d) and 2(h)].<sup>29</sup> The epithelium appears very disorganized, but ducts are readily observed with the remaining alveolar structures [Fig. 2(h), arrowhead]. By involution day 6, all of the alveoli have collapsed and both epithelium and stroma are being rearranged into ducts (Figs. 2(i) and 2(l)). The majority of cell death is finished by involution day 8 to 10 [Figs. 2(j), 2(k), 2(m), and 2(n)] and epithelial structures are back to a normal, nonpregnant, single layer of ductal epithelial cells with lumens (see \* in figure).<sup>29</sup>

Individual nuclei of ductal epithelial cells ( $\wedge$ ) are easily appreciated in H and E stained sections in nonpregnant and mammary lobules as early after lactation as involution day 2, whereas nuclei only begin to be visible as bright white spots with RCM at involution day 6. Milk in the ducts of early involuting glands is reflective in the RCM images, making it difficult to distinguish individual nuclei (dark areas between milk-filled lumens) with RCM, especially during involution. This may be because the milk secretion signal has become increasingly reflective relative to epithelial cell nuclei in the RCM images. Another possibility is that the nuclear chromatin has changed in the early involuting, differentiated epithelial cell nuclei due to elongation of ductal cells compressed by lumens filled with milk [see Fig. 2(g),  $\wedge$ ], such that they can no longer condense with acetic acid treatment. When nuclear contours begin to reappear at involution day 6, nuclei are

better appreciated with RCM. Alternative contrast agents may make it easier to image involuting nuclei. Treatment of a fatty mammary gland [Fig. 2(o)] with Carnoy's fixative [Fig. 2(p)] allows for the distinction between epithelial and fat cells by dramatically reducing the fat cell background [black area devoid of fat surrounding ducts in Fig. 2(p) inset] and allowing for better visualization of ductal epithelial cells. Ductal lumens [Fig. 2(p) inset, \*] are also more readily appreciated with Carnoy's fixative treatment.

### 3.4 Measuring Nuclear Size in Cells from Human Breast Core Needle Biopsies

Measuring the size and chromatin content of epithelial cell nuclei has been proposed as a diagnostic technique for preinvasive neoplasia, because nuclei of early cancer cells are enlarged as compared to those in normal cells.<sup>30</sup> According to the literature, investigators utilizing formalin-fixed histological sections reported the diameter of normal nondysplastic epithelial cell nuclei to be typically 5 to 7  $\mu\text{m}$ . Her2/neu positive and negative epithelial cancer cells were found to be 8.58 to 9.8  $\mu\text{m}$  in diameter according to one study,<sup>31</sup> with others reporting even larger nuclei (10 to 12  $\mu\text{m}$ ).<sup>30,32,33</sup>

To determine if RCM could be used to obtain images for measurements of nuclear size, nuclear size was measured in RCM images from human breast biopsy tissues. A representative RCM image is illustrated in Figs. 3(a) and 3(b). Arrows in Fig. 3(b) indicate representative nuclei with well-differentiated edges, as seen when nuclear size was measured by drawing lines through the nuclei with software on a digital screen. The mean nuclear size for the image pictured is  $5.45 \pm 0.67 \mu\text{m}$  (standard error =  $0.11 \mu\text{m}$ ). All nuclei measured (other data not shown) were well within the range given in the literature.<sup>30-33</sup> However, measurement of all nuclei present within an image could not be performed, because at the current resolution, we could not always distinguish a clear edge to the nucleus. Systems with higher resolution as well as the use of alternative contrast agents are possible means to improve the technique allowing nuclear size to be evaluated as a possible characteristic seen on RCM, which could distinguish benign from malignant breast tissue.

### 3.5 Imaging Human Breast Core Needle Biopsies

Figure 4 shows three examples of human core biopsies that were imaged in entirety by RCM before being processed for routine pathological studies. *x-y* maps of the entire biopsy allow the imager to look at the complete cell patterns of each core, highlighting the heterogeneity of each sample and allowing for areas of interest to be focused on. The biopsies shown in Figs. 4(a) and 4(b) have areas of mammary epithelial cells infiltrating into the surrounding stroma (closed arrows), which were magnified to the right by clicking on the area of interest in the *x-y* map using the RCM software. Figure 4(b) is from the same project as in Fig. 3(a), and the histology is representative of invasive ductal carcinoma according to the H and E review. The core shown in Fig. 4(c) is predominantly collagenous tissue, which is highlighted in the higher magnification panel by the presence of fat cells (open arrows) and stroma (\*).

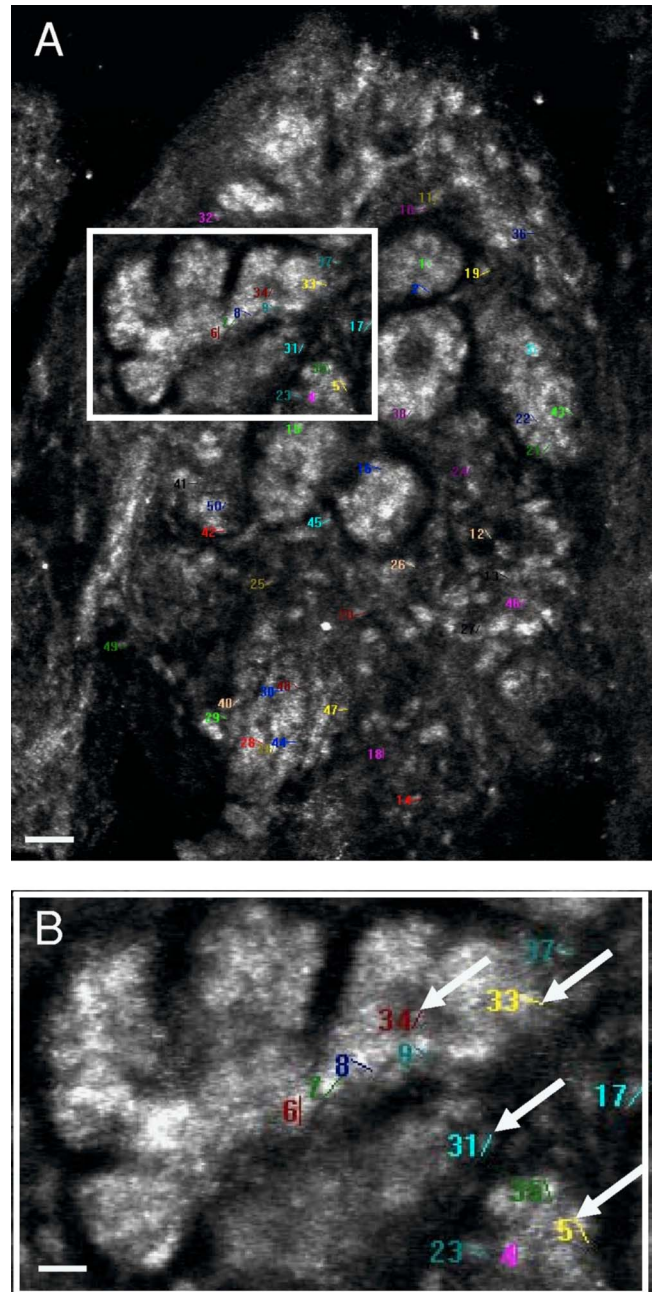


**Fig. 3** Nuclear size measurements can be performed on human breast biopsy tissue imaged by RCM. Representative RCM images of normal mammary epithelial structures in core needle biopsies from one patient in which (a) nuclear size has been measured, with (b) a closeup of the boxed area. Arrows indicate representative nuclei with well-differentiated edges that were measured with the Metamorph software. Magnification: RCM=30 $\times$ , bar (a): 10  $\mu\text{m}$ , bar (b): 50  $\mu\text{m}$ .

### 3.6 Comparing Reflectance Confocal Microscopy and Hematoxylin and Eosin of Pathological Malignant Lesions in Human Breast Core Needle Biopsies

During carcinogenesis, genetic mutations transform normal breast ductal epithelial cells into cancer cells, which may

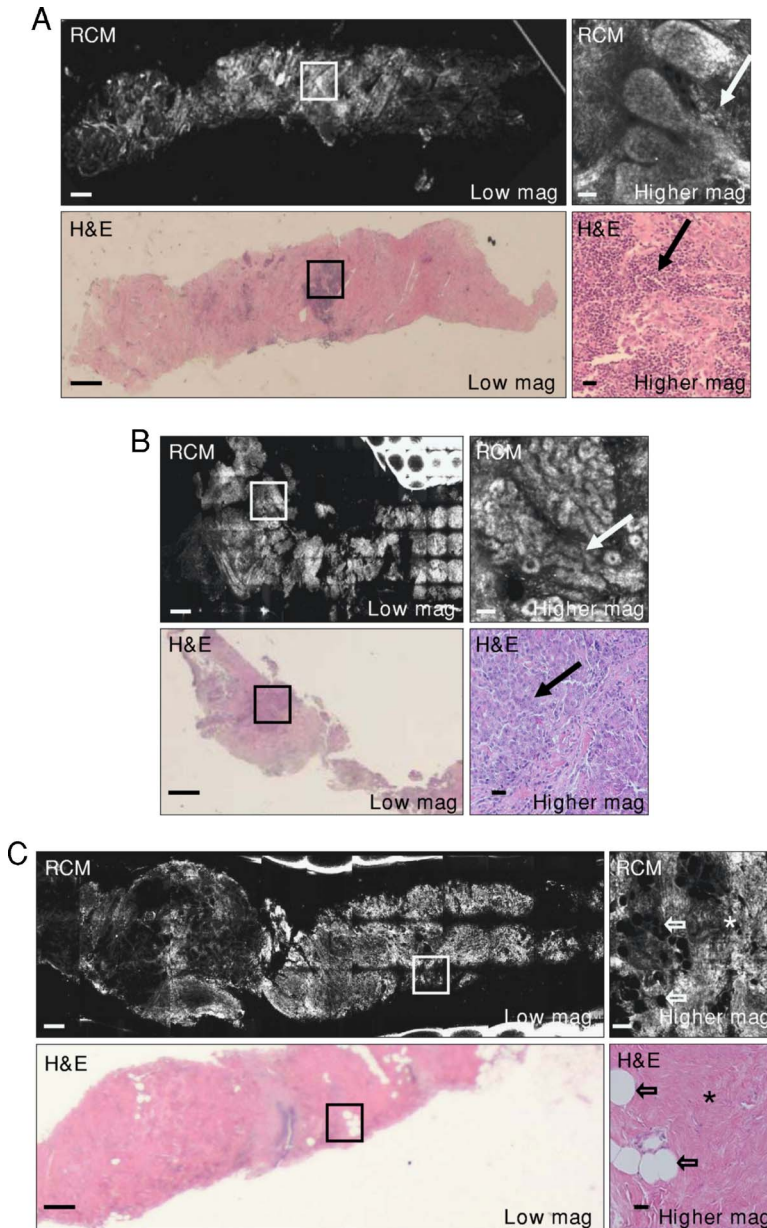


**Fig. 4** RCM can be used to compare with H and E images of human core biopsy tissue. Examples of three human core breast biopsies imaged in entirety by RCM. Boxes in (a) and (b) indicate areas of mammary epithelial cells shown at higher magnification (right panels). The core biopsy specimen in (c) is predominantly collagenous tissue. The area indicated by the box is shown at higher magnification in the right panels. Representative points of interest indicated by closed arrows: cancer cell invasion, open arrows: fat cell nuclei, and \*: stroma. Magnification: H and E: low mag=4 $\times$ , bar: 500  $\mu\text{m}$ ; high mag=20 $\times$ , bar: 50  $\mu\text{m}$ . RCM: low mag=x-y map, bar: 500  $\mu\text{m}$ ; high mag=30 $\times$ , bar: 50  $\mu\text{m}$ .

develop into ductal carcinoma *in situ* (DCIS). DCIS is the stage at which cancer cells have not crossed the basement membrane and are well circumscribed. DCIS may then progress to invasive ductal carcinoma, where cancer cells invade through the basement membrane into the surrounding fat and stroma, where they may attempt to form ductal structures. This differs from invasive carcinoma, which may originate from lobules and is clinicopathologically characterized by small, round cells that infiltrate into the stroma in a single file of cancer cells.<sup>34</sup> Invasive ductal carcinoma, on the other hand, infiltrate in cords.

To determine whether RCM could detect hallmark areas of interest during different stages of human breast cancer development, RCM images from human breast core biopsy tissue were compared with conventional H and E stained sections by first imaging the biopsies with RCM, and on completion formalin-fixing, paraffin-embedding, sectioning, and staining biopsies. Figure 5 shows comparisons of RCM [Figs. 5(a)–5(e)] with H and E [Figs. 5(f)–5(j)] images from benign parenchyma [Figs. 5(a) and 5(f)], DCIS [Figs. 5(b) and 5(g)], *in-situ* and invasive lobular carcinoma [Figs. 5(c) and 5(h)], invasive lobular carcinoma [Figs. 5(d) and 5(i)], and invasive

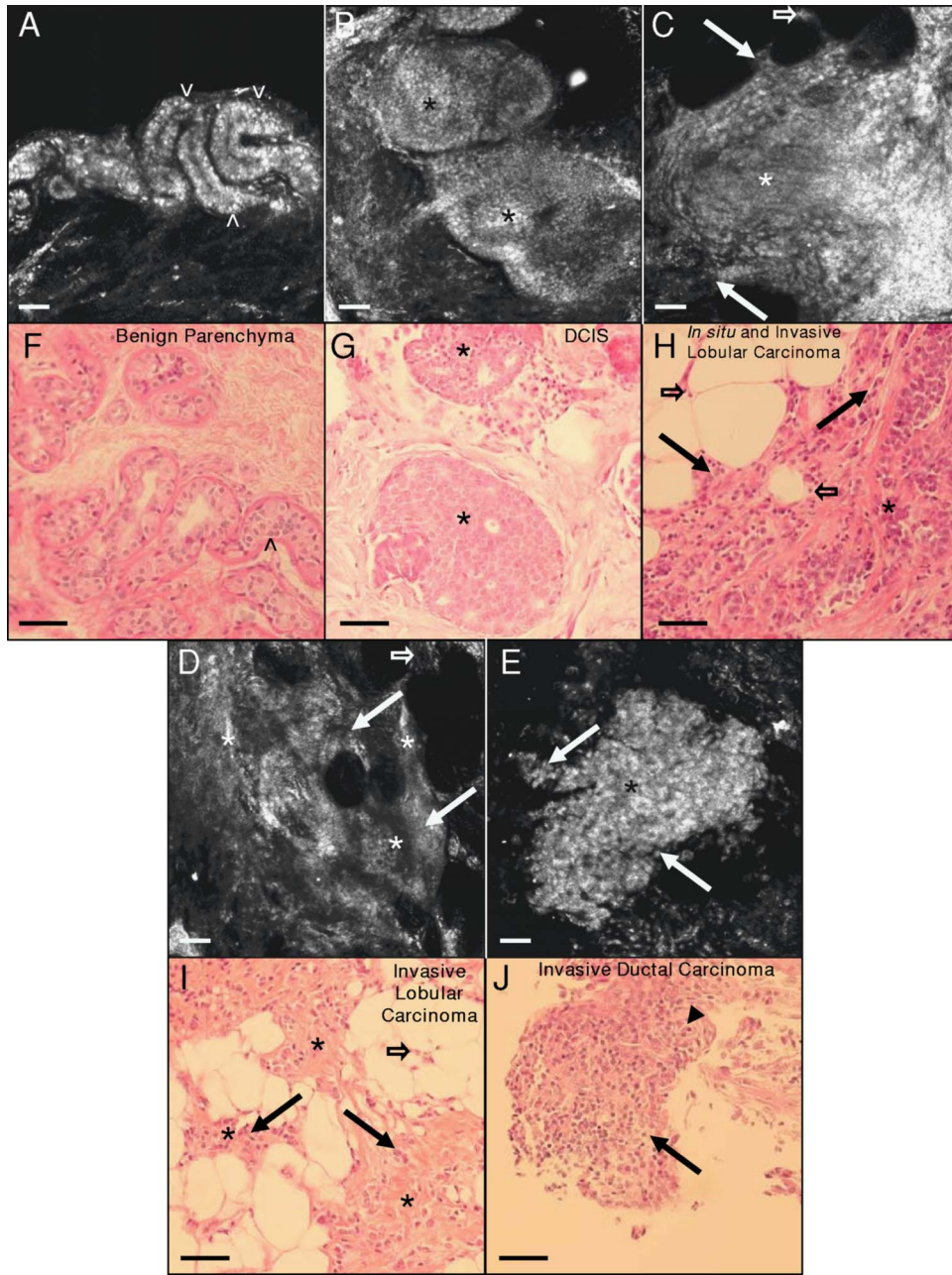


**Fig. 5** RCM can be used to image benign breast parenchyma and malignant lesions in human breast core biopsies. (a) through (e) Comparison of RCM and (f) through (j) H and E images from (a) and (f) benign parenchyma, (b) and (g) ductal carcinoma *in situ* (DCIS) (c) and (h) *in-situ* and invasive lobular carcinoma, (d) and (i) invasive lobular carcinoma, and (e) and (j) invasive ductal carcinoma from human breast biopsies. Representative points of interest indicated by ^: normal epithelial cell nuclei, \*: cancer cell nuclei, closed arrows: cancer cell invasion (linear for invasive lobular carcinoma), arrowhead: cancer cells attempting to form duct, and open arrows: fat cell nuclei. Magnification: H and E=20 $\times$ , bar: 50  $\mu$ m; RCM=30 $\times$ , bar: 50  $\mu$ m.

ductal carcinoma [Figs. 5(e) and 5(j)] from human breast biopsies. Linearly invasive cancers cells can be seen on H and E in Figs. 5(h) and 5(i), and the attempt of cancer cells to form at duct can be seen on H and E in Fig. 5(j, arrowhead). Features of breast biopsies, such as normal epithelial cell nuclei ( $\wedge$ ), cancer cell nuclei (\*), cancer cell invasion (arrows), and fat cell nuclei (open arrows), can be well distinguished in RCM images and correlated well with H and E-stained sections of the biopsy specimens.

### 3.7 Comparing Reflectance Confocal Microscopy and Hematoxylin and Eosin of Benign Histological Features in Human Breast Core Needle Biopsies

In addition to malignant features of the biopsies, other benign attributes present in the biopsies can also be visualized by RCM, such as benign stromal tissue [Figs. 6(a) and 6(b)], which is mainly composed of striations of collagenous tissue

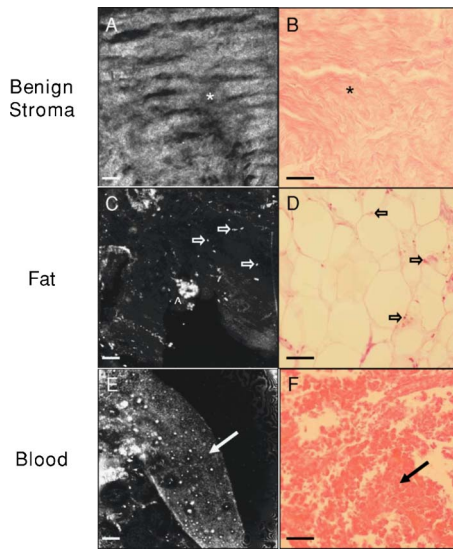


**Fig. 6** RCM can be used to identify and distinguish benign stroma, fat, and blood in human breast core biopsy specimens. (a), (c), and (e) Comparison of RCM, and (b), (d), and (f) H and E images from (a) and (b) benign stroma, (c) and (d) fat, and (e) and (f) blood from human breast core biopsies. Representative points of interest indicated by  $\wedge$ : epithelial cell nuclei,  $*$ : collagenous striations, open arrows: fat cell nuclei, and closed arrows: blood cells. Magnification: H and E=20 $\times$ , bar: 50  $\mu$ m; RCM=30 $\times$ , bar: 50  $\mu$ m.

( $*$ ) and fat cell nuclei (open arrows) in fatty tissue [Figs. 6(c) and 6(d)]. The RCM image of fat is not as homogeneous as the H and E image. These irregularities are characteristic of RCM images of nonepithelial cells, since the imaging method used has been optimized for visualization of epithelial cells, which is illustrated by the clear image of a small epithelial cell cluster ( $\wedge$ ) surrounded by the irregular fat and stroma. Figures 6(e) and 6(f) illustrate the appearance blood cells (arrow) of a blood clot, not an uncommon event found during breast core biopsy sampling.

#### 4 Summary and Significance

Near-infrared (NIR) RCM allows for 3-D optical sectioning of opaque objects in real time. It is already an established diagnostic tool for differentiating between malignant and non-malignant dermatologic conditions, but its utility in the setting of other malignancies remains to be determined. Potential advantages over traditional microscopy include provisions for an immediate determination of tissue specimen adequacy without the need for tissue fixation or staining, as well as for the intraoperative, real-time assessment of tumor margins allowing for complete excision at the time of first surgery. Importantly, the technology allows for nondestructive pathology, such that tissue evaluated by RCM can still be formalin-fixed and paraffin-embedded for routine pathologic and immunohistochemical analyses.

Our work used the current technology to demonstrate the ability to image mouse mammary and human breast ductal structures, to correlate cellular morphology and epithelial/stromal content as seen on routine histology by H and E staining, and to perform reliable immunohistochemical analyses for ER $\alpha$  expression despite prior exposure to acetic acid. In

this study, acetic acid was used to enhance contrast of the cell nucleus by compaction of the chromatin within the cell nucleus due to the extraction of histone proteins, as is well documented in the scientific and patent literature. The compacted chromatin enhances backscattering from the cell nucleus, causing it to appear bright relative to the surrounding tissue. Use of NIR light for imaging allows imaging at deeper depths in the tissue than is possible using visible light. This is due to the fact that visible light suffers from higher scattering and attenuation in tissue than does infrared light. The NIR wavelength used in this study (830 nm) was found to provide a reasonable tradeoff between image resolution and maximum imaging depth when imaging skin, and seems to have worked well in regards to depth, since the biopsies are thin. A lower wavelength may allow for fluorescent tags (which may or may not interfere with subsequent histology and immunohistochemistry), but it may also compromise the depth of penetration. Conversely, a higher wavelength could increase depth but compromise contrast and resolution. The development of new contrast agents and noninterfering tags will probably be more helpful in increasing resolution, detection, and surveillance of cancer cells. This, in turn, will lead to the ability to monitor morphological and biochemical markers of altered proliferation, apoptosis, and differentiation in real time, as well as to noninvasively evaluate the relative contribution of specific molecular pathways throughout the process of carcinogenesis and in response to therapy.

#### Acknowledgments

The authors would like to thank Jay Eastman and Christi Alessi Fox at Lucid, Incorporated, for their expertise and knowledge in the technological aspects of reflectance confocal microscopy. These studies were supported by the Susan G. Komen Breast Cancer Foundation BCTR86106 (Liu, Furth, Sidawy, Makarlou, and Tilli) and the Susan G. Komen Breast Cancer Foundation Post-Doctoral Fellowship Research Award PDF0503642 (Tilli).

#### References

1. W. M. White, G. J. Tearney, B. Z. Pilch, R. L. Fabian, R. R. Anderson, and R. D. Gaz, "A novel, noninvasive imaging technique for intraoperative assessment of parathyroid glands: confocal reflectance microscopy," *Surgery (St. Louis)* **128**, 1088–1100 (2000).
2. V. Campo-Ruiz, E. R. Ochoa, G. Y. Lauwers, and S. Gonzalez, "Evaluation of hepatic histology by near-infrared confocal microscopy: a pilot study," *Hum. Pathol.* **33**, 975–982 (2002).
3. A. L. Clark, A. M. Gillenwater, T. G. Collier, R. Alizadeh-Naderi, A. K. El Naggar, and R. R. Richards-Kortum, "Confocal microscopy for real-time detection of oral cavity neoplasia," *Clin. Cancer Res.* **9**, 4714–4721 (2003).
4. R. A. Drezek, R. Richards-Kortum, M. A. Brewer, M. S. Feld, C. Pitris, A. Ferenczy, M. L. Faupel, and M. Follen, "Optical imaging of the cervix," *Cancer* **98**, 2015–2027 (2003).
5. S. Gonzalez, K. Swindells, M. Rajadhyaksha, and A. Torres, "Changing paradigms in dermatology: confocal microscopy in clinical and surgical dermatology," *Clin. Dermatol.* **21**, 359–369 (2003).
6. S. P. Hicks, K. J. Swindells, M. A. Middelkamp-Hup, M. A. Sifakis, E. Gonzalez, and S. Gonzalez, "Confocal histopathology of irritant contact dermatitis in vivo and the impact of skin color (black vs white)," *J. Am. Acad. Dermatol.* **48**, 727–734 (2003).
7. C. Curiel-Lewandrowski, C. M. Williams, K. J. Swindells, S. R. Tahan, S. Astner, R. A. Frankenthaler, and S. Gonzalez, "Use of in vivo confocal microscopy in malignant melanoma—an aid in diagnosis and assessment of surgical, and nonsurgical therapeutic approaches," *Arch. Dermatol.* **140**, 1127–1132 (2004).

8. K. Swindells, N. Burnett, F. Rius-Diaz, E. Gonzalez, M. C. Mihm, and S. Gonzalez, "Reflectance confocal microscopy may differentiate acute allergic and irritant contact dermatitis in vivo," *J. Am. Acad. Dermatol.* **50**, 220–228 (2004).
9. V. Campo-Ruiz, G. Y. Lauwers, R. R. Anderson, E. Delgado-Baeza, and S. Gonzalez, "In vivo and ex vivo virtual biopsy of the liver with near-infrared, reflectance confocal microscopy," *Mod. Pathol.* **18**, 290–300 (2005).
10. J. S. Sunness, R. A. Schuchard, N. Shen, G. S. Rubin, G. Dagnelie, and D. M. Haselwood, "Landmark-driven fundus perimetry using the scanning laser ophthalmoscope," *Invest. Ophthalmol. Visual Sci.* **36**, 1863–1874 (1995).
11. H. D. Cavanagh, W. M. Petroll, H. Alizadeh, Y. G. He, J. P. McCulley, and J. V. Jester, "Clinical and diagnostic use of in vivo confocal microscopy in patients with corneal disease," *Ophthalmology* **100**, 1444–1454 (1993).
12. W. M. White, M. Rajadhyaksha, S. Gonzalez, R. L. Fabian, and R. R. Anderson, "Noninvasive imaging of human oral mucosa in vivo by confocal reflectance microscopy," *Laryngoscope* **109**, 1709–1717 (1999).
13. M. Huzaira, F. Rius, M. Rajadhyaksha, R. R. Anderson, and S. Gonzalez, "Topographic variations in normal skin, as viewed by in vivo reflectance confocal microscopy," *J. Invest. Dermatol.* **116**, 846–852 (2001).
14. M. Rajadhyaksha, G. Menaker, T. Flotte, P. J. Dwyer, and S. Gonzalez, "Confocal examination of nonmelanoma cancers in thick skin excisions to potentially guide Mohs micrographic surgery without frozen histopathology," *J. Invest. Dermatol.* **117**, 1137–1143 (2001).
15. A. L. Agero, K. J. Busam, C. Benvenuto-Andrade, A. Scope, M. Gill, A. A. Marghoob, S. Gonzalez, and A. C. Halpern, "Reflectance confocal microscopy for in vivo diagnosis of basal cell carcinoma," *J. Am. Acad. Dermatol.* **54**, 638–643 (2006).
16. T. Collier, A. Lacy, R. Richards-Kortum, A. Malpica, and M. Follen, "Near real-time confocal microscopy of amelanotic tissue: detection of dysplasia in ex vivo cervical tissue," *Acad. Radiol.* **9**, 504–512 (2002).
17. A. Gerger, S. Koller, T. Kern, C. Massone, K. Steiger, E. Richtig, H. Kerl, and J. Smolle, "Diagnostic applicability of in vivo confocal laser scanning microscopy in melanocytic skin tumors," *J. Invest. Dermatol.* **124**, 493–498 (2005).
18. S. Nori, F. Rius-Diaz, J. Cuevas, M. Goldgeier, P. Jaen, A. Torres, and S. Gonzalez, "Sensitivity and specificity of reflectance-mode confocal microscopy for in vivo diagnosis of basal cell carcinoma: a multicenter study," *J. Am. Acad. Dermatol.* **51**, 923–930 (2004).
19. C. S. Chen, M. Elias, K. Busam, M. Rajadhyaksha, and A. A. Marghoob, "Multimodal in vivo optical imaging, including confocal microscopy, facilitates presurgical margin mapping for clinically complex lentigo maligna melanoma," *Br. J. Dermatol.* **153**, 1031–1036 (2005).
20. S. Gonzalez, W. M. White, M. Rajadhyaksha, R. R. Anderson, and E. Gonzalez, "Confocal imaging of sebaceous gland hyperplasia in vivo to assess efficacy and mechanism of pulsed dye laser treatment," *Lasers Surg. Med.* **25**, 8–12 (1999).
21. D. Aghassi, R. R. Anderson, and S. Gonzalez, "Time-sequence histologic imaging of laser-treated cherry angiomas with in vivo confocal microscopy," *J. Am. Acad. Dermatol.* **43**, 37–41 (2000).
22. A. Parrish, E. Halama, M. T. Tilli, M. Freedman, and P. A. Furth, "Reflectance confocal microscopy for characterization of mammary ductal structures and development of neoplasia in genetically engineered mouse models of breast cancer," *J. Biomed. Opt.* **10**, 051602 (2005).
23. M. Rajadhyaksha, G. Menaker, and S. Gonzalez, "Confocal microscopy of excised human skin using acetic acid and crossed polarization: rapid detection of non-melanoma skin cancers," *Proc. SPIE* **3907**, 84–88 (2000).
24. M. Rajadhyaksha and J. M. Zavislan, "Confocal laser microscope images tissue in vivo," *Laser Focus World* **33**, 5–8 (1997).
25. A. Fraschini, C. Pellicciari, M. Biggiogera, and M. G. Manfredi Romanini, "The effect of different fixatives on chromatin: cytochemical and ultrastructural approaches," *Histochem. J.* **13**, 763–769 (1981).
26. C. L. Smithpeter, A. K. Dunn, R. A. Drezek, T. G. Collier, and R. R. Richards-Kortum, "Near real time confocal microscopy of cultured amelanotic cells: sources of signal, contrast agents and limits of contrast," *J. Biomed. Opt.* **3**, 429–436 (1998).
27. M. D. Abramoff, P. J. Magelhaes, and S. J. Ram, "Image processing with ImageJ," *Biophotonics Int.* **11**, 36–42 (2004).
28. M. T. Tilli, M. S. Frech, M. E. Steed, K. S. Hruska, M. D. Johnson, J. A. Flaws, and P. A. Furth, "Introduction of estrogen receptor-alpha into the TTA/TAg conditional mouse model precipitates the development of estrogen-responsive mammary adenocarcinoma," *Am. J. Pathol.* **163**, 1713–1719 (2003).
29. M. M. Richert, K. L. Schwertfeger, J. W. Ryder, and S. M. Anderson, "An atlas of mouse mammary gland development," *J. Mammary Gland Biol. Neoplasia* **5**, 227–241 (2000).
30. V. Backman, M. B. Wallace, L. T. Perelman, J. T. Arendt, R. Gurjar, M. G. Muller, Q. Zhang, G. Zonios, E. Kline, J. A. McGilligan, S. Shapshay, T. Valdez, K. Badizadegan, J. M. Crawford, M. Fitzmaurice, S. Kabani, H. S. Levin, M. Seiler, R. R. Dasari, I. Itzkan, J. Van Dam, and M. S. Feld, "Detection of preinvasive cancer cells," *Nature (London)* **406**, 35–36 (2000).
31. X. Sastre-Garau, P. Genin, A. Rousseau, A. Al Ghuzlan, A. Nicolas, P. Freneaux, C. Rosty, B. Sigal-Zafrani, J. Couturier, J. P. Thiery, H. Magdelenat, and A. Vincent-Salomon, "Increased cell size and Akt activation in HER-2/neu-overexpressing invasive ductal carcinoma of the breast," *Histopathology* **45**, 142–147 (2004).
32. N. Wang, B. G. Stenkvist, and B. Tribukait, "Morphometry of nuclei of the normal and malignant prostate in relation to DNA ploidy," *Anal Quant Cytol. Histol.* **14**, 210–216 (1992).
33. K. Sokolov, L. T. Nieman, A. Myakov, and A. Gillenwater, "Polarized reflectance spectroscopy for pre-cancer detection," *Technol. Cancer Res. Treat.* **3**, 1–14 (2004).
34. G. Arpino, V. J. Bardou, G. M. Clark, and R. M. Elledge, "Infiltrating lobular carcinoma of the breast: tumor characteristics and clinical outcome," *Breast Cancer Res. Treat.* **6**, R149–R156 (2004).